Biosensors and Bioelectronics 128 (2019) 61–67

Contents lists available at ScienceDirect

Biosensors and Bioelectronics

journal homepage: www.elsevier.com/locate/bios

Imaging-based fluorescent sensing platform for quantitative monitoring and visualizing of fluoride ions with dual-emission quantum dots hybrid

Jian Zhang[a], Jingjing Qian[b], Qingsong Mei[c], Lei Yang[d], Lifang He[a], Shengjun Liu[a], Cheng Zhang[a], Kui Zhang[a,*]

[a] School of Chemistry and Chemical Engineering, Anhui University of Technology, Ma'anshan, Anhui 243032, China
[b] Department of Applied Chemistry, Anhui Agricultural of University, Hefei, Anhui 230036, China
[c] School of Biological and Medical Engineering, Hefei University of Technology, Hefei, Anhui 230009, China
[d] Department of Chemistry, University of North Carolina at Chapel Hill, Chapel Hill, NC 27599, United States

ARTICLE INFO

Keywords:
Fluoride ions
Ratiometric
Fluorescence
Quantum dots
Smartphone imaging

ABSTRACT

Herein, a ratiometric fluorescence sensing strategy coupled with smartphone imaging-based sensing platform was proposed for the on-site determination of fluoride ion (F^-) with high sensitivity and accuracy. The principle of sensing strategy is based on the fluoride-promoted Si–O bond cleavage of 2-(*tert*-butyldiphenylsilyloxy)phenol (2-TBDPSP) to release 2-hydroxyphenolate, which rapidly auto-oxidized to *ortho*-quinone. As excellent electron acceptor, these quinone species covalently bonded on the surface of dual-emission amino-modified quantum dots (QDs) nanohybrid *via* a Michael's type adduction, quenching the fluorescence of green-emitting QDs on the surface of the nanohybrid, while not affecting the fluorescence of red-emitting QDs embedding silica nanospheres. Upon exposure to different amounts of F^-, the variations of dual emission intensity ratios display continuous color changes from green to red, which could be directly observed by naked eyes. Then a smartphone imaging-based sensing platform was constructed by 3D-printing technology. The smartphone camera acquired the images of fluorescence derived from samples, and the Color Picker APP installed in smartphone continued to read out the Red, Green and Blue (RGB) channel values of these images. There was a linear relationship between the ratio of Red and Green (R/G) and F^- concentration in the range of 0–70.0 μM. The limit of detection (LOD) was estimated to be 2.0 μM, much lower than the allowable level of F^- (~63.16 μM) in drinking water set by World Health Organization. This methodology reported here is low-cost, portable, easy-operation, and thus potentially attractive for F^- determination without the need of elaborate equipment.

1. Introduction

As the smallest anion with a high charge density, fluoride ions (F^-) has arisen as an attractive target for sensor designs due to its intimate association with our human health. An appropriate amount of fluoride in drinking water can help prevent dental caries and strengthen bones, but there are a number of adverse effects that intake excessive fluoride, including dental fluorosis, skeletal fluorosis, urolithiasis, increased rates of bone fractures, decreased birth rates, impaired thyroid function, and lower intelligence in children (Cittanova et al., 1996; Horowitz, 2003; Oszvath, 2009). In order to prevent such problems, the World Health Organization recommends the optimal fluoride level at 0.7–1.2 mg/L^{-1} in drinking water. Although the highly sensitive and accurate fluoride ion assays can be achieved by conventional laboratory testing, these methods are time-consuming, require sophisticated analytical instrumentations, well-trained personnels, and complex pretreatments or enrichment processes (Guimarães et al., 2009; Nie et al., 2017; Rocha et al., 2013; Zhang et al., 2017). For example, prior to use, fluoride ion selective electrode as an efficient analytical tool for the determination of F^- should be soaked in ultrapure water for several hours and then keep flushing with ultrapure water until the blank potential was below 300 mV. Fluorescence-based sensors are attracting more and more attention due to its unique capability for target assays by our naked eye on the variations of fluorescence brightness or color to overcome the above-mentioned concern (Zhou et al., 2016). Guin's group utilized a green, water-dispersible photoluminescence "on-off-on" probe of CdTe QDs-MPA/Eu^{3+} for the colorimetric fluorescent determination of F^- from vapors generated by hydrofluoric acid (Singh et al., 2017). Singhal et al. also demonstrated the successful used of CQDs/Eu^{3+} probe for selective and sensitive F^- detection (Singhal

* Corresponding author.
E-mail address: zhangkui@mail.ustc.edu.cn (K. Zhang).

https://doi.org/10.1016/j.bios.2018.12.044

Available online 29 December 2018
0956-5663/

et al., 2017). Li et al. reported a single nanofluorophore “off-on” probe based on the unique fluoride-boron interaction to achieve the naked eye visual determination of environmental F^- (Li et al., 2018). However, only rely on our naked eye are not able to achieve satisfactory sensitivity and accuracy, because our eyes are not efficacious to distinguish the slight fluorescent variations for revealing trace amounts of analyte. Therefore, there still exists a great demand to develop a simple, low-cost, easy-operation fluorescence sensor to reliable assay of fluoride ions with high sensitivity and accuracy for improving drinking water safety.

Recently, smartphones are increasingly important as a portable sensing platform for the on-site detection, owing to their relatively portable, low cost, increasing the suitability of data acquisition and processing power (Edwards et al., 2017; McGonigle et al., 2018). One promising strategy is to integrate an attachment that allow the built-in smartphone high-quality camera to function as the optical sensor for digital imaging readout, such as smartphone microscopes (Lee and Yang, 2014), fluorescence readers (Yu et al., 2014), test strip readers (Mei et al., 2016), microfluidic chip readers (Barbosa et al., 2015), and colorimetric readers (Kwon et al., 2016; Wang et al., 2017). Ozcan's group developed a field-portable fluorescence microscopy platform installed on a smartphone for fluorescence imaging of isolated 100 nm particle as well as individual human cytomegalovirus (Wei et al., 2013). Roda et al. reported, for the first time, the use of a smartphone to image and quantify biochemiluminescence to detect total bile acids and cholesterol in biological fluids (Roda et al., 2014). All these cases, the smartphone have proved their efficacy as an alternative imaging-based sensing platform to perform functions equivalent to much larger and more expensive laboratory instruments. However, the smartphone imaging-based sensing platform based on the fluorescence quenching or enhancing effect at one certain wavelength generally suffer from the unavoidable disturbance induced by intensity fluctuations, which could ascribe to the instrumental or environmental factors (Sun et al., 2016). On the contrary, the methods based on ratiometric fluorescence could eliminate most of the ambiguities by self-calibration of two or more different emission bands (Yao et al., 2013). Furthermore, the ratiometric sensing methods provided a wider fluorescent color variation for smartphone camera imaging, which would be rewarded by high sensitivity and accuracy (Lee et al., 2017).

Therefore, a novel method that combined the merits of ratiometric fluorescence sensing strategy and the smartphone imaging-based sensing platform was proposed for F^- detection with high sensitivity and accuracy. We previously synthesized the dual-emission cadmium telluride quantum dots nanohybrid (rQDs@SiO_2@gQDs), in which red-emitting ones (rQDs) are embedded in silica nanospheres as reference and green-emitting ones (gQDs) are covalently linked onto the silica nanospheres surface as a signal report unit. Then, dual-emission nanohybrid have been further functionalized with *p*-mercaptoaniline (*p*MA) to obtain amino modified rQDs@SiO_2@gQDs (rQDs@SiO_2@gQDs-NH_2) nanohybrid *via* the simple coordination bonding between -SH group of *p*MA and cadmium ions of gQDs. The addition of F^- promoted the Si-O cleavage of 2-(*tert*-butyldiphenylsilyloxy)phenol to release 2-hydroxyphenolate. The auto-oxidation of 2-hydroxyphenolate modulates the fluorescence of rQDs@SiO_2@gQDs-NH_2 nanohybrid from green to red through an effective electron transfer (ET) process. Then, the constructed smartphone imaging-based sensing platform acquires the fluorescent images of these color variations and readout the corresponding red, green, and blue (RGB) channel values of these obtained images by the built-in Color Picker APP. By using digital image colorimetry, there was a linear relationship between the ratio of R/G values and F^- concentrations in the range from 0 to 70.0 μM, and the limit of detection (LOD) was estimated to be 2.0 μM. Meanwhile, the smartphone imaging-based sensing platform also exhibits high sensitivity and accuracy in the detection of F^- in actual samples.

2. Experimental section

2.1. Chemicals and materials

3-Aminopropyltriethoxysilane (APTS), 4-aminothiophenol (4-ATP), 1,2-benzenediol, *tert*-butylchlorodiphenylsilane, 1-(3-dimethylaminopropyl)-3-ethylcarbodiimidehydrochloride (EDC) and *tert*-butylchlorodiphenylsilane were supplied by Aladdin reagent Co., Ltd. (Shanghai, China). The other reagents were purchased from Sinopharm Chemical Reagent Company, Ltd. (Shanghai, China). All reagents were used as received without further purification.

2.2. Synthesis of 2-(tert-butyldiphenylsilyloxy)phenol (2-TBDPSP)

To a chilled (0 °C) solution of 1,2-benzenediol (0.55 g, 5.0 mmol) in anhydrous CH_3CN (20 mL) added triethylamine (0.8 mL) and a solution of *tert*-butylchlorodiphenylsilane (1.38 g, 5.0 mmol) in CH_3CN (10 mL). The mixture was stirred at room temperature for 2.5 h and then diluted with EtOAc (150 mL). The organic layer was washed (brine, 3 × 50 mL), dried ($MgSO_4$), and concentrated. Flash silica gel column chromatography (1:10 EtOAc/hexanes) purification of the residue gave 1.26 g (3.6 mmol, 72%) as a transparent viscous liquid.2-(*tert*-butyldiphenylsilyloxy)phenol (2-TBDPSP):^{1}H NMR (400 MHz, $CDCl_3$) δ ppm 7.89 (dd, J = 7.89, 1.46 Hz, 4H), 7.45–7.58 (m, 6H), 7.12 (dd, J = 7.89, 1.46 Hz, 1H), 6.90 (td, J = 7.60, 1.75 Hz, 1H), 6.52–6.64 (m, 2H), 6.00 (s, 1H), 1.29 (s, 9H); ^{13}C NMR (101 MHz, $CDCl_3$) δ ppm 147.0, 142.5, 135.5, 132.0, 130.4, 128.2, 122.3, 120.0, 118.5, 115.1, 26.8, 19.6.

2.3. Detection of fluoride ions in aqueous solution

The detail of synthesized red-emitting QDs embedding in silica nanospheres (rQDs@SiO_2-NH_2) and dual-emission amino functional green-emitting QDs coated rQDs@SiO_2 (rQDs@SiO_2@gQDs-NH_2) nanohybrid were provided in the Supporting information. In ten comparison tubes, different volumes of F^- standard solution (1 mM) were injected into 200 μL of 10 μM 2-TBDPSP solution. After 30 min reaction, the mixtures were diluted to 1.80 mL with carbonate buffer solution (pH = 9.0, 5.0 mM). Then, 200 μL of the as-synthesized dual-emission rQDs@SiO_2@gQDs-NH_2 nanohybrid was added respectively. The mixture was shaken thoroughly at room temperature prior to fluorescence measurement. The final concentrations of F^- in the ten tubes were 0, 2.5, 5, 7.5, 12.5, 17.5, 27.5, 45, 70, and 107.5 μM, respectively. Followed by shaking for 10 min, the fluorescence spectra of all the mixtures were measured by a fluorescence spectrophotometer (G9800A, Agilent Cary Eclipse) excited at 365 nm. The color variations were observed under a UV lamp (excitation wavelength at 365 nm).

2.4. Fabrication of smartphone imaging-based sensing platform for F^- detection in actual sample

To fabricate smartphone imaging-based sensing platform, a 3D model device were designed by using of CAD program, and the relevant specs were then imported into a 3D printer. Finally, the accessory device was printed out by using thermoplastic black acrylonitrile butadiene styrene polymer as the ink. The accessory device mainly contains four parts: (1) was a lamp holder for ultraviolet (UV) light emitting diode (LED) excitation light source, (2) was a quart cuvette with round grooves for sample solution, (3) an optical filter (400–700 nm) was placed between the sample cell and the smartphone to prevent the excitation light entering into camera, and (4) was the dark cavity opened an optical window with the diameter of 1.5 cm to contact with phone camera. The UV-LED excitation light source (365 nm excitation, maximum 3 W output power) was soldered onto a printed circuit board, adjoined to an aluminium block for heat dissipation, and powered by a 3 V battery. The four parts were then glued together with an iPhone 6 as the smartphone imaging-based sensing platform.

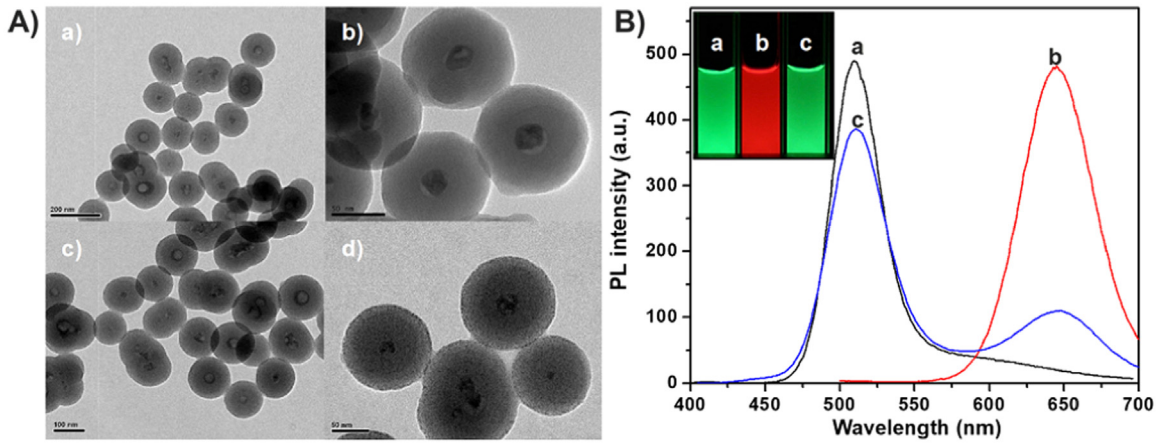

Fig. 1. A) Transmission electron microscopy (TEM) images of: (a) and (b) rQDs@SiO_2-NH_2 nanospheres; (c) and (d) rQDs@SiO_2@gQDs-NH_2 nanohybrid at low and high magnification, respectively. B) The fluorescence spectra of (a) gQDs nanoparticles, (b) rQDs@SiO_2-NH_2 nanospheres, and (c) rQDs@SiO_2@gQDs-NH_2 nanohybrid.

The lake water samples were obtained from a local lake and filtered twice using 0.22 μm filter paper to remove the solid suspensions. The later water samples were diluted 5 times with ultrapure water so that the level of F^- was within the linear ranges. The spiked concentrations of actual samples were 10, 20 and 50 μM. Followed the same assay process as described in Section 2.3, the resulted solution (250 μL) was directed added into the quart cuvette after complete reaction, and then inserted into the dark cavity. The solution in the cuvette was excited and produced fluorescence by UV LED in the lamp holder. Then, the smartphone iPhone 6 camera captured the images of the produced fluorescence from the cuvette. The Color Picker APP installed in the smartphone analysed the color of the images and converted the color into the RGB data within one second. The ratio of R and G values was calculated to be used as a parameter for F^- quantification to construct a standard curve by OriginPro 8 on a desktop computer.

3. Results and discussion

As shown in Fig. 1A-a and b, the nearly monodispersed rQDs@SiO_2-NH_2 nanospheres have multiple red emissive QDs nanocrystal cores with an average size of about 114.04 ± 16 nm. The average diameter of rQDs@SiO_2@gQDs-NH_2 nanohybrid were determined to be 118.81 ± 16 nm without the obvious different from the original rQDs@SiO_2-NH_2 nanospheres as shown in Fig. 1A-c and d. However, rQDs@SiO_2-NH_2 nanospheres surfaces are very smooth and rQDs@SiO_2@gQDs-NH_2 nanohybrid surfaces are comparatively rough, suggesting the successful attachment of the gQDs nanoparticles on the rQDs@SiO_2-NH_2 nanospheres surfaces. Compared with rQDs@SiO_2@gQDs nanohybrid, the FT-IR spectrum of rQDs@SiO_2@gQDs-NH_2 nanohybrid exhibit new distinct absorption bands at 1633, 1493, 1282 and 1177 cm^{-1} (see Fig. S1 in the Supporting information), which can be attributed to the N-H bending vibration, skeleton vibration of aromatic ring, C-N stretching vibration and in-plane vibration of aromatic ring. These results suggested that the *p*MA were successfully combined with the dual-emission rQDs@SiO_2@gQDs nanohybrid surface to obtain amino modified rQDs@SiO_2@gQDs nanohybrid.

The gQDs exhibited a maximum absorption peak at ~480 nm (see Fig. S2 in the Supporting information) and a strong fluorescent emission peak at 508 nm (seen in Fig. 1 B). The rQDs@SiO_2-NH_2 nanospheres showed a fluorescent maximum at 648 nm. In contrast, UV–vis absorption peak of rQDs@SiO_2@gQDs-NH_2 nanohybrid slightly shifted from 480 to 475 nm, likely due to the damping effect of the -SH anchoring group from green-emitting QDs surface (Sreenivasan et al., 2013). Despite the shift in UV–vis absorption, the fluorescence spectrum of rQDs@SiO_2@gQDs-NH_2 nanohybrid displayed well-resolved dual emission bands at 508 and 648 nm under a single excitation at 365 nm. The rQDs@SiO_2@gQDs-NH_2 nanohybrid exhibited similar green color to gQDs, while significantly different from the rQDs@SiO_2-NH_2 nanospheres. These dual-emission characteristics of rQDs@SiO_2@gQDs-NH_2 nanohybrid have demonstrated their potential in ratiometric fluorescence sensing system. The stability of rQDs@SiO_2@gQDs-NH_2 nanohybrid against time is systematically investigated by flashing UV light (Fig. S3) in an aqueous solution. After 8 consecutive illuminations at 365 nm (15 min for each time), the relative fluorescence intensity has no apparent change, implying the photostability of dual-emission QDs nanohybrid that is long enough for further use in the detection.

Given the large difference between Si-O and Si-F bond dissociation energy (69 and 141 kcal/mol, respectively), the fluoride-promoted Si-O cleavage reaction has been widely used in the design of fluoride-selective optical sensors (Zhou et al., 2014). Scheme 1 illustrates the principle of ratiometric fluorescence sensing strategy for the detection of F^- based on the rQDs@SiO_2@gQDs-NH_2 nanohybrid. As the high chemical affinity of F^- to silicon atom, the addition of F^- triggered the cleavage of the Si-O of 2-(*tert*-butyldiphenylsilyloxy)phenol (2-TBDPSP) to release 2-hydroxyphenolate, which rapidly auto-oxidized to*ortho*-quinone at pH = 9.0. The quinone species were then covalently bonded with the surface of rQDs@SiO_2@gQDs-NH_2 nanohybrid *via* a Michael's type adduction (Li et al., 2017), and then the electron transfer access (ET) was turned on due to the efficient electron acceptance of quinone (Wang et al., 2018). Thus, as shown in Fig. 2A, these quinine species effectively quenched the fluorescence of gQDs on the surface of rQDs@SiO_2@gQDs-NH_2 nanohybrid, whereas the intensity of rQDs still remained constant for the coated of silica shell. Meanwhile, the changes of fluorescence intensity ratio of rQDs@SiO_2@gQDs-NH_2 nanohybrid led to a noticeable color change from green to red. However, only addition of 2-TBDPSP or F^- did not influence the fluorescence spectrum and color, which clearly demonstrated the validity of our proposed mechanism. The mechanism was further evidenced using ESI-MS spectroscopy. After F^- were mixed with 2-TBDPSP, the deprotonated 1,2-benzenediol (2-hydroxyphenolate) peak at m/z = 108.70 and *tert*-butylfluorodiphenylsilane peak at m/z = 258.09 were clearly detected (Fig. 2B-b), suggesting the Si–O bond cleavage of 2-TBDPSP to form a more stable structure for the stronger coordinative ability of Si-F bond than the Si–O bond. When *p*MA were mixed with 1,2-benzenediol at pH = 9.0, the peak of protonated amino-quinone peak at m/z = 232.16 and sodiation amino-quinone complex peak at m/z = 255.10indicated that the *ortho*-quinone could covalently bond with amino group of rQDs@SiO_2@gQDs-NH_2 nanohybrid *via* the Michael's type adduct reaction. Meanwhile, A theoretical calculation was carried out with Gaussian09 for understanding the electron transfer process also shown

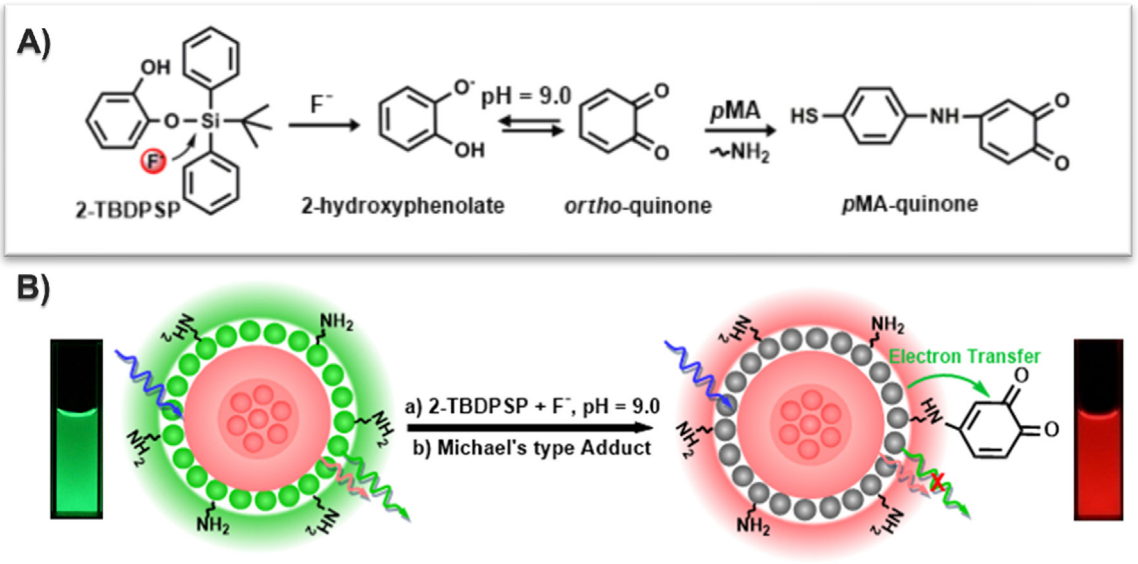

Scheme 1. A) The reaction process of 2-TBDPSP with F^- and *p*MA at pH = 9.0, and the chemical structure of 2-TBDPSP, 2-hydroxyphenolate, *ortho*-quinone and *p*MA-quinone. B) The principle of the ratiomatric fluorescence strategy for the detection of F^- by the dual-emission amino-modified QDs nanohybrid.

in the Fig. S4.

2-TBDPSP can be hydrolysed at low pH values, and the fluorescence of rQDs@SiO_2@gQDs-NH_2 nanohybrid can be quenched at high pH conditions (see Fig. S5). On the other hand, the fluorescence quenching of gQDs on the surface of rQDs@SiO_2@gQDs-NH_2 nanohybrid occurred more and more rapid with the increase of pH from 7.0 to 9.5 (see Fig. S6). At pH 9.0, the time needed of F^- detection reached a minimum of about 30 mins. Therefore, the carbonate buffer (pH = 9.0, 5.0 mM) was chosen as the optimal pH for F^- detection in the further experiments. Under the optimal conditions, the fluorescence intensity at 508 nm of the rQDs@SiO_2@gQDs-NH_2 nanohybrid gradually decreased with increasing the concentrations of F^-, while the fluorescence intensity at 648 nm remained constant as illustrated in Fig. 3A. Even if F^- concentration was as low as 2.50 μM, the fluorescence intensity ratio of $(I_{648}/I_{508})_0/(I_{648}/I_{508})$ was still decreased ~13.1%. With a further increase of F^- concentration to 27.50 μM, the fluorescence intensity ratio was decreased ~77.50%, and was proportional to the F^- concentration as shown by the highly linear calibration plot with standard deviation R = 0.9746. When the concentration of F^- was larger than 27.50 μM, the fluorescence intensity ratio was strongly decreased and was also proportional to the F^- concentration with R = 0.9871. The evolution of fluorescence intensity ratio is very suitable for the determination of F^- within a very wide range of 0–107.50 μM in two consecutive linear ranges. Owing to the variation in the PL intensity, a series of noticeable color changes from green to green-yellow, yellow, orange, and red were observed from the rQDs@SiO_2@gQDs-NH_2 nanohybrid colloids under a UV lamp (Fig. 3B). Therefore, the visual recognition of F^- by the naked eye under a UV lamp is feasible. Meanwhile, these color variations have been further confirmed by Commission Internationale de L'Eclairage (CIE) coordinates in Fig. 3C and Table S1. The sensing system had green emission with CIE coordinates of (0.2752, 0.5268). As the F^- concentrations increased, a substantial red-shift tendency in the CIE coordinate was observed from green (0.2807, 0.5153; 2.50 μM) to green-yellow (0.3092, 0.4904; 7.50 μM), yellow (0.3725, 0.4473; 17.50 μM), orange (0.4763, 0.3995; 40.0 μM), red (0.5532, 0.3509; 70.0 μM) and dark red (0.5796, 0.3217; 107.5 μM). These results indicated that the reliable of color variation in the ratiometric fluorescence sensing system from another aspect.

To examine the selectivity of the ratiometric fluorescence sensing system, the fluorescence intensity ratios (I_{648}/I_{508}) of rQDs@SiO_2@

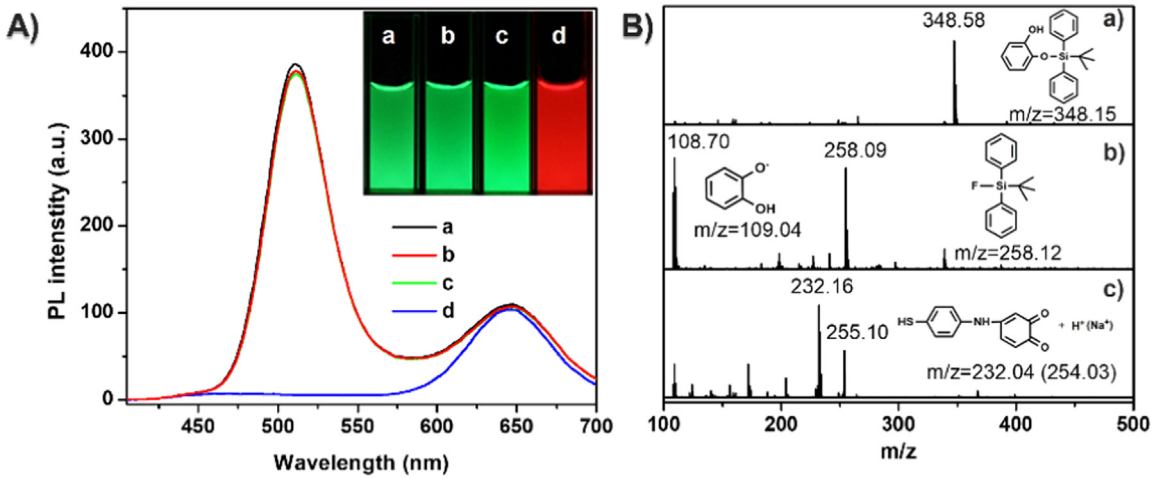

Fig. 2. A) Fluorescence spectra of (a) rQDs@SiO_2@gQDs-NH_2 nanohybrid, (b) rQDs@SiO_2@gQDs-NH_2 nanohybrid in the presence of 2-TBDPSP, (c) rQDs@SiO_2@gQDs-NH_2 nanohybrid in the presence of F^-, (d) rQDs@SiO_2@gQDs-NH_2 nanohybrid in the presence of 2-TBDPSP and F^- at pH = 9.0, respectively. B) ESI-MS spectra of the mixtures of 2-TBDPSP (a) with F^- (b), and 1,2-benzenediol with *p*-mercaptoaniline (*p*MA) at pH = 9.0 (c) in aqueous solution, respectively.

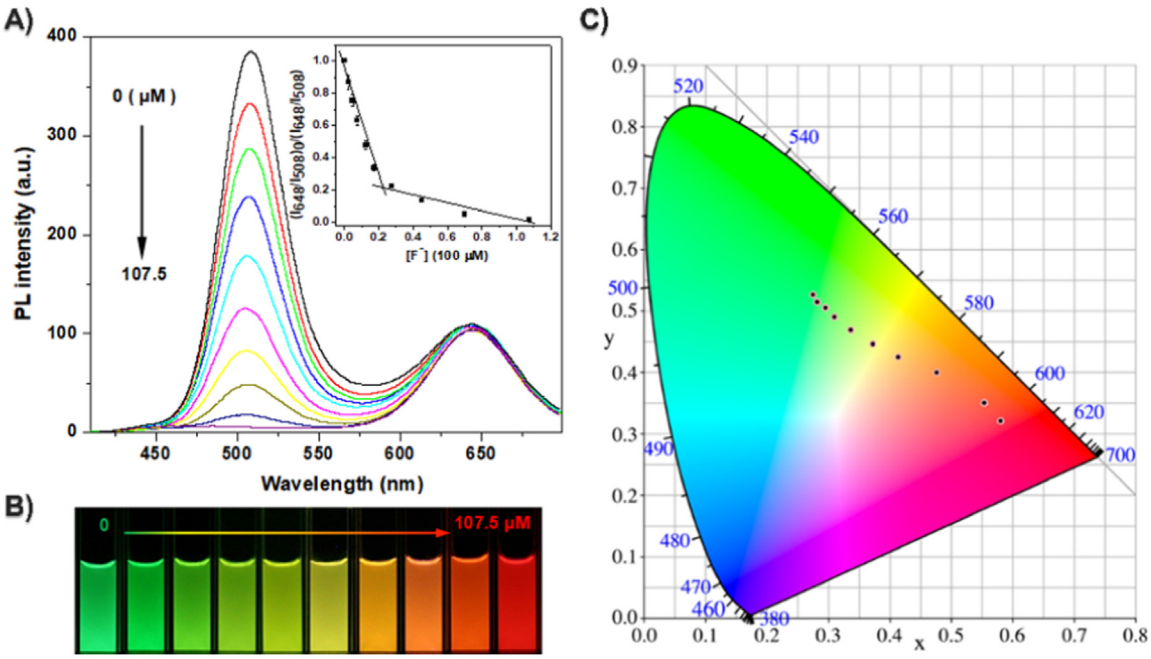

Fig. 3. (A) The fluorescence spectra of the ratiometric sensing system with increasing of the concentrations of F^-. The inset was the linear plot of the fluorescence intensity ratio $(I_{648}/I_{508})_0/(I_{648}/I_{508})$ *versus* the concentration of F^-. $(I_{648}/I_{508})_0$ and (I_{648}/I_{508}) were the fluorescence intensity ratio of the sensing system in the absence and presence of F^-, respectively. (B) Corresponding fluorescence photographs of the above-mentioned solution taken under a 365 nm UV illumination. (C) CIE 1931 (x,y) chromaticity diagram of the sensing system for the detection of F^- at different concentrations derived from fluorescence spectra (black circles).

gQDs-NH_2 nanohybrid were carefully evaluated in the addition of common anions without and with the coexistence fluoride ions, including Cl^-, Br^-, I^-, HCO_3^-, CO_3^{2-}, HPO_4^{2-},NO_3^-, SO_4^{2-}, SCN^- and S^{2-}. In Fig. S7 (black bars), the results showed that only F^- causes significant fluorescence intensity ratios response (I_{648}/I_{508} = 17.65) to the rQDs@SiO_2@gQDs-NH_2 nanohybrid, while other anions do not affect the fluorescence (I_{648}/I_{508} < 0.32). Furthermore, an interference experiment was conducted to examine the interference of coexisting anions (as shown in Fig. S6-strip bars). Clearly, the fluorescence response of the sensing system toward F^- is scarcely interfered by the coexisting anions even the concentrations of the interference anions are 50 times higher than that of F^-. These above observations reveal that the high selective of this ratiometric fluorescence sensing system to F^- determination. It should be noted that the addition of Cu^{2+} and Fe^{2+} can inhibit the *ortho*-quinone formation in our sensing system due to the strong coordination ability of Cu^{2+} and Fe^{2+} to 2-hydroxyphenolate, and thus bring interferences for F^- detection in real water samples (Fig. S8A). As for Cu^{2+} and Fe^{2+}, their interference can be easily suppressed by a simple sample pretreatment with S^{2-} because Cu^{2+} and Fe^{2+} can promptly form insoluble CuS and FeS with S^{2-}. After the simple pretreatment, the fluorescence responses of our sensing system to the single fluoride ions solution and to the pretreated mixture solution of fluoride ions with Cu^{2+} and Fe^{2+} were nearly the same (Fig. S8A). Meanwhile, we also found that the ClO^- could also quench the fluorescent signal of gQDs on the surface of rQDs@SiO_2@gQDs-NH_2 nanohybrid to a certain extent (see Fig. S8B). Fortunately, the interference caused by ClO^- could be ignored because it is generally not present in lake water system due to its highly instability and oxidizing ability.

However, the application of above fluorescence method was limited in the on-site determination of actual samples for requiring the complex fluorophotometer. Meanwhile, our eyes' sensitivity is not enough to distinguish the slight color variations for the quantitative fluoride ions detection, especially for the revealing of trace amounts of F^- (0–5 μM). To overcome this problem, we designed a simple, portable and cost-effective detection device by using smartphone as an optical signal reader (as shown in Fig. 4A) to recognize and output the fluorescence color changes of the samples. The internal structure of the imaging-based sensing platform was also provided in Fig. S9. The F^- detection process with the smartphone imaging-based sensing platform has been showed in Fig. 4B. After warming for 5 min (optimized in Fig. S10), the ultraviolet light from the UV lamp focused on the cuvette of the sample cell. The sample solution in the cuvette was excited to produced fluorescence. The smartphone camera captured the images of the produced fluorescence as shown in Fig. 4C. The Color Picker APP installed in the smartphone analysed the images' color and converted into the RGB data within one second. The home page and the data recording interface of Color Picker were also shown in Fig. S11. Different from Lee's methodology, the reacted microarray was fluorescence imaging at each of green and red channel with the bandpass filters (λ_{em} = 520/10 nm and λ_{em} = 605/15 nm), and then all images were analysed with ImageJ on a desktop computer. Our smartphone imaging-based sensing platform could directly output all the red, green and blue (RGB) channels values of fluorescence images with Color Picker APP, eliminating the inevitable intensity fluctuation of multi-measurements.

However, an approach of directly converting RGB values into the corresponding analyte concentrations sometimes does not yield satisfactory results. As illustrated in Fig. S12, the blue channel values exhibit no discernible trend and are difficult to correlate with fluoride ions concentration. Meanwhile, the red or green channel values show an obviously intensity fluctuations in the dark color areas, resulting in a narrow linear range or poor correlation coefficient. In contrast, the intensity ratio of red and green channels intensity is proportional increased to the F^- concentration in the range of 0–70 μM as shown in the Fig. 4D. The linear fitting equation is R/G = 5.0333 C + 0.2730 (C: 100 μM) with the correlation coefficient of 0.9881. The lowest of detectable concentration (LOD) was estimated to be 2.00 μM based on the three times standard deviation of the blank signal (Roda et al., 2014; Zhang et al., 2014; Yao et al., 2013), which was much lower than the maximum residue limit defined by World Health Organization (63.16 μM). This method displayed a broader linear range and its LOD is comparable to or even much lower than the reported values observed in most of the existed fluorescence nanosensors listed in Table S2.

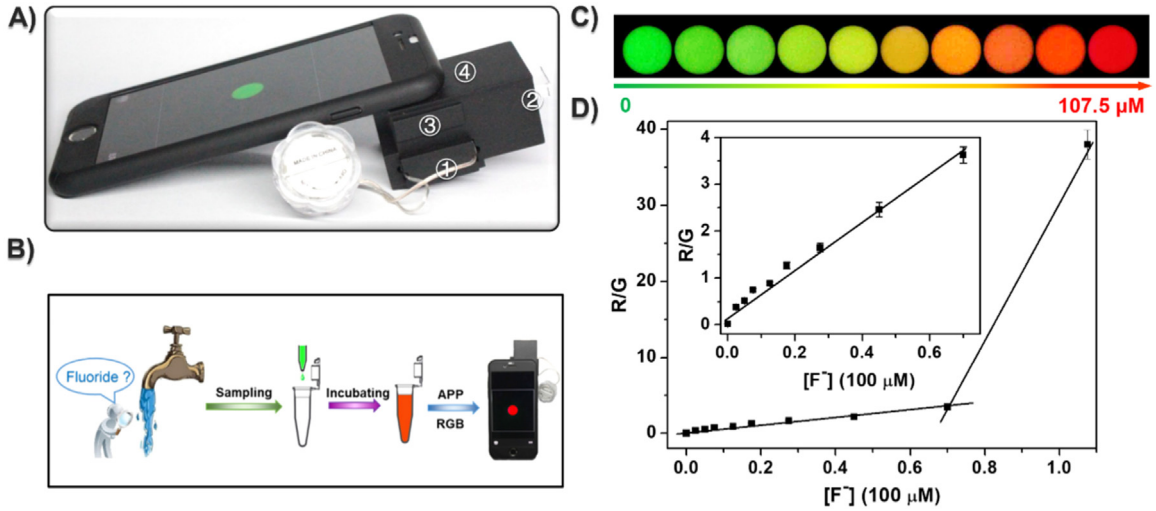

Fig. 4. (A) Picture of the smartphone imaging-based sensing platform. (B) Steps for detecting F^- by using of smartphone-based sensing platform. (C) The luminescent images of testing system upon additions of different amounts of F^-, which were directly taken by the smartphone digital camera. (D) The color change and the ratio of R/G values *versus* F^- concentration in the range of 0–107.50 μM. The inset figure is linear relationship of mean luminescent intensities with F^- concentrations from 0 to 70 μM. (For interpretation of the references to color in this figure legend, the reader is referred to the web version of this article.)

Table 1
Determination and recovery test of F^- in complex environmental samples from lake water.

Sample	Found by IC Method (μmol/L)	Found by Smartphone Based Device (μmol/L)[a]	Spike (μmol/L)	Measure (μmol/L)	Recovery (%)	RSD (%)
①	18.1	3.81	10.0	13.28	94.37	2.65
			20.0	24.71	104.46	4.47
			50.0	57.26	106.86	5.78
②	22.6	4.90	10.0	14.78	98.91	3.31
			20.0	24.13	96.16	4.49
			50.0	57.41	104.21	4.82
③	24.0	5.22	10.0	15.33	101.17	3.26
			20.0	26.26	104.96	4.67
			50.0	53.69	96.93	5.69

[a] The F^- concentrations were obtained after a total of 5 times dilution with ultrapure water.

Though its performance was not as excellent as the methods reported by Zhang's group (Chen et al., 2016), our ratiometric sensing strategy provided a wider fluorescent color variation from green to dark red with the increasing of F^- concentration for smartphone camera imaging, which was rewarded by high sensitivity and accuracy. Moreover, the low-cost, portable, easy-operation advantage of the constructed smartphone imaging-based sensing platform is more attractive than previously reported methods without the need of elaborate equipment especially in the extreme poverty areas.

In order to verify the usefulness of this method, the concentrations of F^- in the blank and spiked actual samples were determined by using the proposed smartphone imaging-based sensing platform. The standard recovery experiments were also carried out. Finally, the determination results were compared with those by ion chromatography (IC) method. As shown in Table 1, the results obtained from the smartphone imaging-based portable platform were in accordance with those from the ion chromatography (IC) method. The recovery of F^- ranged from 94.37% to 106.86% and the RSD (n = 3) was in the range of 2.65–5.78%. All the experimental results confirmed that the smartphone imaging-based sensing platform had a high accuracy, reliability, and sensitivity to meet the on-site determining requirements of F^- in practical applications.

4. Conclusions

In summary, we have presented a novel ratiometric fluorescence sensing method for quantitative monitoring and visualizing of F^- based on smartphone imaging-based portable platform. Our developed method possesses many advantages, such as excellent anti-interference ability, portable feasibility, and easy-operation. On the other hand, the detection only needs a very little amount of sample, and is very simple and inexpensive compared to earlier methods. This smartphone imaging-based sensing platform could hugely improve the accessibility of F^- detection even in resource-limited contexts especially in the extreme poverty areas.

Acknowledgments

This work is supported by Science and National Natural Science Foundation of China (No. 21507134, 21675158, 21675038, 61603001), the Fundamental Research Funds for the Central Universities (Grant nos. 2014HGCH0002 and JZ2016YYPY0042).

Appendix A. Supporting information

Supplementary data associated with this article can be found in the online version at doi:10.1016/j.bios.2018.12.044.

References

Barbosa, A.I., Gehlot, P., Sidapra, K., Edwards, A.D., Reis, N.M., 2015. Biosens. Bioelectron. 70, 5–14.
Chen, X.C., Yu, S.M., Yang, L., Wang, J.P., Jiang, C.L., 2016. Nanoscale 8, 13669–13677.
Cittanova, M.L., Lelongt, B., Verpont, M.C., 1996. Anesthesiology 84, 428–435.
Edwards, P., Zhang, C., Zhang, B., Hong, X., Nagarajan, V., Yu, B., Liu, Z., 2017. Sci. Rep. 7, 12224–12230.
Guimarães, I.C., Rezende, C.C., Silva, J.A.F., Jesus, D.P., 2009. Talanta 78, 1436–1439.
Horowitz, H.S., 2003. J. Public. Health Dent. 63, 3–8.
Kwon, L., Long, K.D., Wan, Y., Yu, H., Cunningham, B.T., 2016. Biotechnol. Adv. 34, 291–304.
Lee, W.I., Shrivastava, S., Duy, L.T., Kim, B.Y., Son, Y.M., Lee, N.E., 2017. Biosens. Bioelectron. 94, 643–650.
Lee, S.A., Yang, C., 2014. Lab Chip 14, 3056–3063.
Li, Y., Guo, A., Chang, L., Li, W.J., Ruan, W.J., 2017. Chem. Eur. J. 23, 6562–6569.
Li, Y.J., Sun, Q., Su, L., Yang, L.L., Zhang, J., Yang, L., Liu, B.H., Jiang, C.L., Zhang, Z.P., 2018. RSC Adv. 8, 8688–8693.
Mei, Q.S., Jing, H.R., Li, Y., Yisibashaer, W., Chen, J., Li, B.N., Zhang, Y., 2016. Biosens. Bioelectron. 75, 427–432.
McGonigle, A.J., Wilkes, T.C., Pering, T.D., Willmott, J.R., Cook, J.M., Mims, F.M., Parisi,

A.V., 2018. Sensors 18, 223–237.
Nie, L., Zhang, Q., Hu, L., Liu, Y.M., Yan, Z.Q., 2017. Sens. Actuators B-Chem. 245, 314–320.
Oszvath, D.V., 2009. Rev. Environ. Sci. Biotechnol. 8, 59–79.
Rocha, R.A., Rojas, D., Clemente, M.J., Ruiz, A., Devesa, V., Velez, D., 2013. J. Agric. Food Chem. 61, 10708–10713.
Roda, A., Michelini, E., Cevenini, L., Calabria, D., Calabretta, M.M., Simoni, P., 2014. Anal. Chem. 86, 7299–7304.
Singh, P., Prabhune, A.A., Tripathi, C.S.P., Guin, D., 2017. ACS Sustain. Chem. Eng. 5, 982–987.
Singhal, P., Vats, B.G., Jha, S.K., Neogy, S., 2017. ACS Appl. Mater. Interfaces 9, 20536–20544.
Sreenivasan, V.K.A., Zvyagin, A.V., Goldys, E.M., 2013. J. Phys. Condens. Mater. 25, 194101–194123.
Sun, J.Y., Mei, H., Wang, S.F., Gao, F., 2016. Anal. Chem. 88, 7372–7377.
Wei, Q., Qi, H., Luo, W., Tseng, D., Ki, S.J., Wan, Z., Go¨ro¨cs, Z., Bentolila, L.A., Wu, T.T., Sun, R., Ozcan, A., 2013. ACS Nano 7, 9147–9155.
Wang, Y.J., Zeinhom, M.M.A., Yang, M.M., Sun, R.G., Wang, S.F., Smith, J.N., Timchalk, C., Li, L., Lin, Y.H., Du, D., 2017. Anal. Chem. 89, 9339–9346.
Wang, G.L., Yuan, F., Gu, T.T., Dong, Y.M., Wang, Q., Zhao, W.W., 2018. Anal. Chem. 90, 1492–1497.
Yao, J.L., Zhang, K., Zhu, H.J., Ma, F., Sun, M.T., Yu, H., Sun, J., Wang, S.H., 2013. Anal. Chem. 85, 6461–6468.
Yu, H., Tan, Y.F., Cunningham, B.T., 2014. Anal. Chem. 86, 8805–8813.
Zhou, Y., Zhang, J.F., Yoon, J., 2014. Chem. Rev. 114, 5511–5571.
Zhou, Y.J., Huang, X.Y., Liu, C., Zhang, R.L., Gu, X.L., Guan, G.J., Jiang, C.L., Zhang, L.Y., Du, S.H., Liu, B.H., Han, M.Y., Zhang, Z.P., 2016. Anal. Chem. 88, 6105–6109.
Zhang, J.J., Chen, S.H., Tan, X.R., Zhong, X., Yuan, D.H., Cheng, Y.F., 2014. Biotechnol. Lett. 35, 1835–1841.
Zhang, J., He, L., Chen, P., Tian, C., Wang, J., Liu, B.H., Jiang, C.L., Zhang, Z.P., 2017. Nanoscale 9, 1599–1606.